

RSC Advances



This is an *Accepted Manuscript*, which has been through the Royal Society of Chemistry peer review process and has been accepted for publication.

Accepted Manuscripts are published online shortly after acceptance, before technical editing, formatting and proof reading. Using this free service, authors can make their results available to the community, in citable form, before we publish the edited article. This *Accepted Manuscript* will be replaced by the edited, formatted and paginated article as soon as this is available.

You can find more information about *Accepted Manuscripts* in the [Information for Authors](#).

Please note that technical editing may introduce minor changes to the text and/or graphics, which may alter content. The journal's standard [Terms & Conditions](#) and the [Ethical guidelines](#) still apply. In no event shall the Royal Society of Chemistry be held responsible for any errors or omissions in this *Accepted Manuscript* or any consequences arising from the use of any information it contains.

ARTICLE

Hierarchically Designed ZnO Nanostructures Based High Performance Gas Sensors

Cite this: DOI: 10.1039/x0xx00000x

Mohammad R. Alenezi,^a T. H. Alzanki,^a A. M. Almeshal,^a A. S. Alshammari,^b M. J. Beliatas,^c S. J. Henley^c and S. R. P. Silva^c

Received 00th January 2012,

Accepted 00th January 2012

DOI: 10.1039/x0xx00000x

www.rsc.org/

Rationally controlled multistage hydrothermal methods have been developed to prepare different types of hierarchical zinc oxide (ZnO) nanostructures with high surface-to-volume ratios and more exposed polar facets. Four types of hierarchical ZnO nanostructures, nanobrushes (ZNBs), nanoleaves (ZNLs), hierarchical nanodisks (HNDs) and nanoflakes (ZNFs) assembled from initial mono-morphological nanostructures, nanowires (ZNWs) and nanodisks (ZNDs), were produced from sequential nucleation and growth following a hydrothermal process. Hierarchical nanostructures with 1D nanowire and 2D nanodisk building blocks were realized using zinc nitrate and zinc sulphate as the source of zinc ions, respectively. Compared to their initial mono-morphological counterparts, the grown hierarchical nanostructures demonstrated superior gas sensing properties. ZNLs and ZNFs showed significant improvement in sensitivity and fast response to acetone. In addition to the high surface-to-volume ratio due to the ultrathin sheet building blocks, the enhanced gas sensing properties of ZNLs and ZNFs are chiefly ascribed to the increased proportion of exposed (0001) polar facets. The current study offers the path for structure induced development of gas sensing properties by designing a necessary nanostructure, which could be used to fabricate high performance nanostructured gas sensors based on other metal oxides.

Introduction

The attention toward hierarchical structures with one-dimensional (1D) or two-dimensional (2D) nanostructure building blocks have grown significantly in recent years because of the extraordinary physical and chemical properties of these structures.¹⁻⁴ They can be utilized in a variety of applications in the bottom-up production of high performance devices.⁵⁻⁸ Gas sensors are significantly important and their development could impact many important fields, including industrial process control, safety systems, disease diagnoses, and environmental monitoring. For instance, sensing low concentration levels of acetone is an effective way to diagnose type-I diabetes.⁹ Therefore, it is greatly required to develop suitable methods to sense low concentrations of acetone.

High temperature growth techniques have been used commonly to produce hierarchical ZnO nanostructures, such as NW arrays,¹⁰ nanohelices,¹¹ nanopropeller,¹² and tower-like nanocolumns.¹³ But, these techniques suffer from many disadvantages and limitations like impurities in the final products, substrates that can be used, high temperatures (~ 500-1100 °C) and vacuum conditions. One can clearly see that the economic feasibility for large scale production is limited, which encouraged researchers to develop low temperature cost

effective growth solution phase methods to produce these nanostructures at large scale.¹⁴⁻¹⁶ Despite all these attractive features of the solution phase methods in growing mono-morphological nanostructures, using these methods to produce hierarchical architectures with rational control over the morphology and size is still challenging.

Herein, we develop an elegant nucleation and growth strategy to synthesize a wide range of hierarchical ZnO nanostructures, nanobrushes (ZNBs), hierarchical nanodisks (HZNDs), nanoleaves (ZNLs) and nanoflakes (ZNFs) by sequentially using zinc nitrate and zinc sulphate as sources of Zn²⁺ in the growth solution. This two-step growth tactic gives a chance to tune and optimize of experimental conditions step by step and provides an opportunity for rational design and synthesis of controlled architectures in nanostructures. The role of morphology and structure of the hierarchical ZnO nanostructures in their performance as gas sensors is investigated. The results indicate that the grown ZNLs and ZNFs display significant improvement in acetone sensing in comparison to other grown nanostructures. These results are explained using photoluminescence (PL) studies. The enhancement in the sensitivity of the gas sensor is ascribed to more active centers that are obtained from the enhanced oxygen

vacancy defects on the hierarchical nanostructures as a result of the increased surface-to-volume ratio and the increased population of unconventional (0001) polar facets.

Experimental

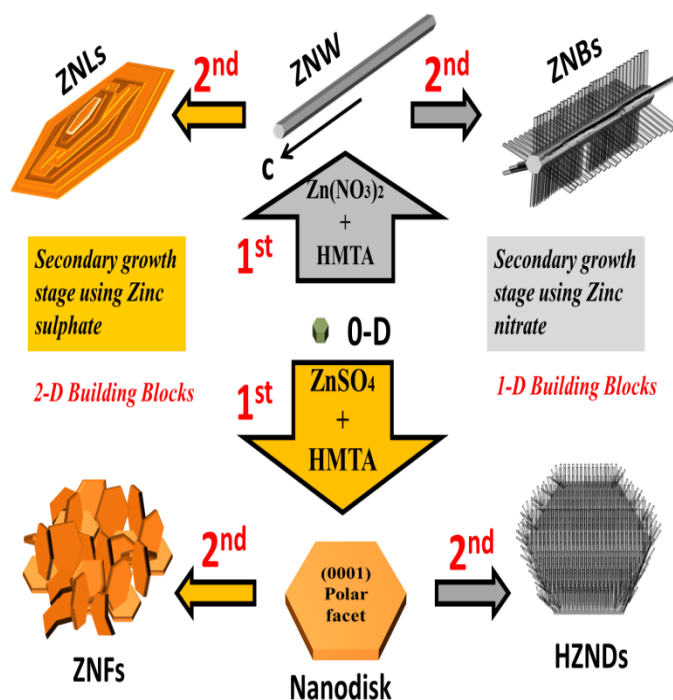
All reagents in this work were analytical grade. The synthesis of ZNWs was described in previous report.¹⁶ Briefly, a seeded silicon (Si) substrate was placed in vial containing a 15 mL growth solution consisting of 25-50 mM zinc nitrate, 12.5-25 mM HMTA, 0.35-0.45 M ammonium hydroxide and 5 mM polyethylenimine (PEI) (end-capped, molecular weight 800 g/mol LS, Aldrich). The vial was covered and then placed in an oven which had been preheated to 90 °C for 24 h. After that, the substrate was then rinsed with DI water and dried in air at 150 °C for 30 min. Then, the ZNWs were uniformly suspended in deionized water (20 mL) in an ultrasonic bath.

The synthesis of ZNDs was also described in previous report.¹⁵ To prepare the ZNDs, a 15 mL vial of the growth solution consisting of 100 mM zinc sulphate (ZnSO_4) and 100 mM HMTA was placed in an oven and heated to 75 °C for 3 hours. Then, the grown nanostructures are filtered and washed thoroughly with ethanol and distilled in water in sequence.

ZNBs and HZNDs were synthesized by using initial ZNWs and ZNDs as seeds in the second growth stage, respectively. A suspension of the initial ZNWs or the ZNDs was mixed with fresh growth solution like the one used to grow the ZNWs initially. The vial containing the mixture was kept at 90 °C for 5 h. Finally, the grown products were washed thoroughly with ethanol and distilled in water in sequence, and dried at 80 °C.

ZNLs and ZNFs were synthesized by using initial ZNWs and ZNDs as seeds in the second growth stage, respectively. A suspension of the initial ZNWs or the ZNDs was mixed with fresh growth solution of (100 mM) zinc sulphate (ZnSO_4) and (100 mM) HMTA. The mixture was then transferred to a vial and heated to 75 °C in an oven for 3 hours. After that, the grown nanostructures are filtered and washed thoroughly with ethanol and distilled in water in sequence. The controlled multistage hydrothermal synthesis to produce different hierarchical nanostructures is depicted in scheme 1.

The crystal structure of the as-prepared products were analyzed through the powder X-ray diffraction (XRD) using a Panalytical X-pert diffractometer with Cu $K\alpha$ radiation. The morphology and crystal structure of as-prepared products were observed by (SEM) using Philips XL-20 scanning electron microscope at 10 kV. Scanning transmission electron microscopy (STEM) and electron diffraction measurements were performed on a Hitachi HD2300A microscope, operating at 200 kV. STEM samples were prepared by depositing a drop of diluted suspension of the nanostructure in ethanol on a carbon film coated copper grid. Photoluminescence (PL) spectroscopy was performed at room temperature using a Cary Eclipse spectrometer with an excitation wavelength of 325 nm. Nitrogen adsorption-desorption isotherms were measured using a surface area analyzer (QUADRASORB SI) at 77 K. The Brunauer-Emmett-Teller (BET) method was applied to calculate surface areas of ZnO nanostructures.



Scheme 1. Summary of the impact of the used zinc counterions in each growth stage on the final morphology of the produced ZnO nanostructure.

Nanostructured gas sensors were fabricated by spin coating solutions containing ZnO nanostructures onto SiO_2/Si substrates with pre-patterned gold electrodes. The gas sensing properties were measured using a home-made gas chamber attached to a Keithley 4200 semiconductor analyzer.

The sensor response, S_g , is defined as $S_g = (I_g - I_a)/I_a$, where I_g is the sensor current value in tested gas environment and I_a is the current value in air. The measurements were performed under fixed bias. The response time, t_r , is defined as the time required for the current to reach 90% of the equilibrium value after injecting the gas, and the recovery time, t_d , is defined as the time necessary for the sensor to return to 10% above the original current value in air after releasing the gas from the test chamber.

Results and discussion

Morphology and structure

Figures 1(a) and 1(b) show SEM image of an array of ZNWs and a single ZNW connecting two gold electrodes, respectively. The corresponding selected area electron diffraction (SAED) pattern of the ZNWs is shown in figure 1(c). ZNWs are single crystal growing along the [0001] direction and their side surfaces are nonpolar $\{10\bar{1}0\}$ planes. An SEM image and the corresponding SAED pattern of a single ZND is shown in figures 1(d) and 1(e), respectively. Most of the exposed facets in the morphology of the ZND are the polar [0001] facets. The XRD patterns of the as-grown ZNWs and ZNDs are shown in the bottom and top of figure 1(f), respectively. The patterns indicate that the produced materials are of high crystallinity and

represent the hexagonal wurtzite-type ZnO (JCPDS No. 36-1451).

Hydrothermally grown ZnO nanostructures usually take the one-dimensional form because the crystal growth rate is higher in [0001] direction.¹⁷ In our previous study we found that different counter-ions of zinc often lead to producing different crystallite morphologies.¹⁸ For the nanodisks, the 2D structure is a result of anisotropic growth, where the sideways growth is faster than the axial growth. The charge of the (0001) facet consisting of Zn^{2+} ions is positive. Consequently, the (0001) surface can adsorb the zinc counter-ions (SO_4^{2-}) in the growth system instead of the hydroxyl anions. As a result, $[\text{Zn}(\text{OH})_4]^{2-}$ needed for the growth are prohibited from attaching onto the (0001) surface and the nanostructure is forced to grow sideways instead of the intrinsically anisotropic growth of along the (0001) direction.¹⁸

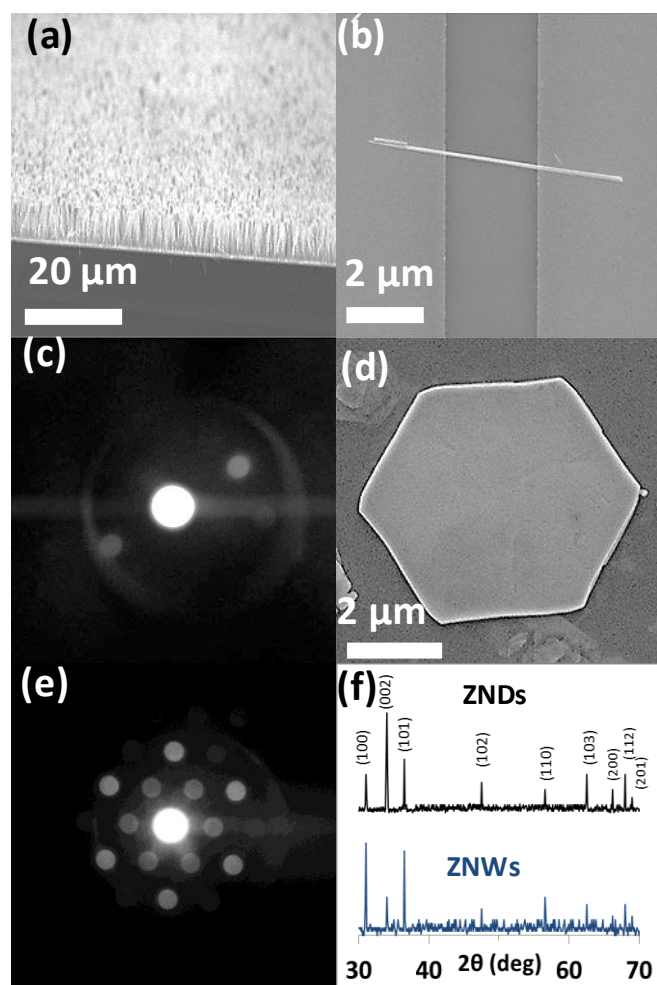


Figure 1. (a) SEM image of a ZNW array, (b) SEM image of a single ZNW, (c) the corresponding SAED pattern of the ZNWs, (d) SEM image of a single ZND, (e) the corresponding SAED pattern of the ZNDs, and (f) the XRD pattern of ZNWs (bottom) and ZNDs (top).

SEM images at different magnifications of a single ZNB are shown in figures 2(a)-(c). It is clear that the secondary NWs are

organizing themselves into regular arrays establishing a 6-fold symmetry (figure 2(c)). The secondary NWs in the ZNBs grow on the side surface of a core NW along the [0001] direction. In the hydrothermal growth system, heterogenous nucleation is much easier than the homogenous one because the interfacial energy between crystal nuclei and substrates is smaller than that between crystal nuclei and solutions.¹⁸ Therefore, secondary NWs can grow on the core ZNW.

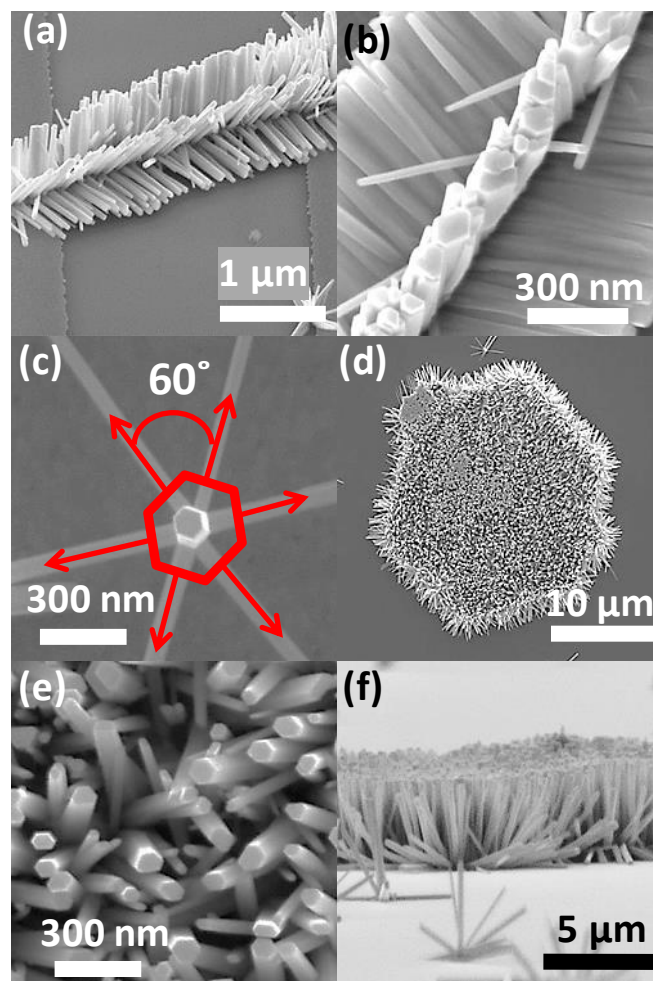


Figure 2. (a) Low magnification, (b) high magnification, and (c) top view SEM image of a single ZNB; (d) low magnification top view, (e) high magnification top view, and (f) side view SEM image of single HZND.

ZNDs were also used as seeds to grow hierarchical ZnO nanostructures, HZNDs. Top and side view SEM images of a single HZND are presented in figures 2(d)-(f). Other SEM images (not shown here) show that the secondary NWs are grown on both the top and the bottom of the 2D initial ZNDs as well as the sides. The secondary NWs are grown along the c-axis with their side surfaces being the nonpolar planes as evident in the high magnification top view SEM image in figure 2(e). More careful observation to this SEM image show that all secondary NWs have a flat bottom at the top, which is the polar (0001) facet. In a different experiment, the ZNDs were

annealed on Si substrate prior to growth; as a result the growth only occurred on the top and side surfaces of the ZNDs and could not grow on the base of the NZDs as shown in figure 2(f). Figures 3(a)–(c) depict SEM images of the ZNLs at different magnifications. From these SEM images we observe that the initial NW was forced to continue growing sideways exposing its [0001] polar facets. Figures 3(d)–(f) show SEM images of a single ZNF grown from initial ZND using ZnSO_4 as the source of Zn^{2+} ions in the secondary growth process. The growth conditions in the secondary stage were similar to those used in the synthesis of the initial ZNDs. From the low magnification SEM image in figure 3(d), we can see that each initial ZND was transformed into a group of flake-like nanostructures or nanoflakes (ZNFs). In the higher magnification SEM images, shown in figures 3(e)–(f), it is evident that these ZNFs are connected together and grown from the same initial ZND. Unlike the ZNBs and HZNDs with many secondary NWs, the building blocks in the ZNLs and ZNFs are ultra-thin ZnO sheets with polar exposed facets as shown in the SEM images.

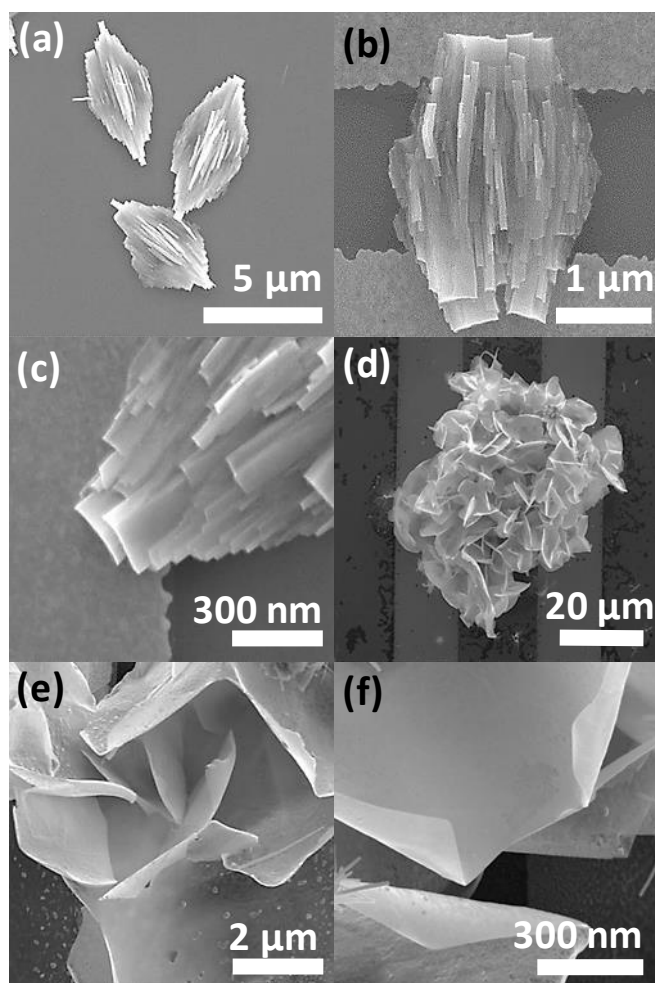
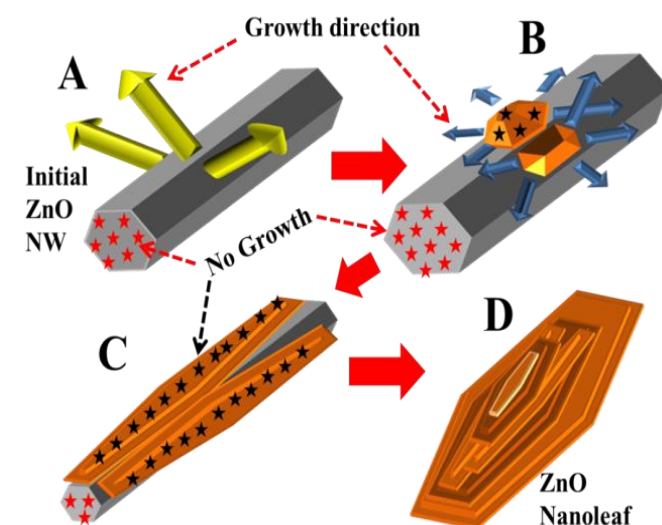


Figure 3. (a) Low magnification, (b) high magnification, and (c) top view SEM image of a single ZNB; (d) low magnification SEM image of a group of ZNLs, (e) medium magnification, and (f) high magnification SEM image of single ZNL.

In growth processes to produce ZNWs, ZNBs and HZNDs with zinc nitrate being used as the source of Zn^{2+} in the growth solution we observed the formation of 1D nanostructures due to the faster crystal growth along the [0001] direction. However, the case was different when the source of Zn^{2+} in the growth solution was changed to zinc sulphate, which led to the production of ZNLs and ZNFs. There are reports in the literature stating that different counter-ions of zinc often lead to producing different crystallite morphologies.¹⁸

In the present case, the shape of the ZNLs is due to anisotropic growth in the second growth stage, where the lateral growth rate is much greater than the growth rate in the c -axis direction as depicted in **scheme 2**. The effective charge on the outermost layer of the (0001) facet consisting of Zn^{2+} ions is positive. Thus, the counter-ions (SO_4^{2-}) in the second growth solution could be adsorbed on the (0001) surfaces, substituting for hydroxyl anions and hindering the attachment of growth units of $[\text{Zn}(\text{OH})_4]^{2-}$ onto the (0001) polar facets of the initial ZNWs (Stage A of scheme 2). Consequently, the intrinsically anisotropic growth of ZnO along the (0001) direction is substantially suppressed and crystal growth then proceeds sideways. New ZnO structures start to grow on the nonpolar sides of the initial ZNW. The growth of the secondary nanostructures is in (0001) direction from the nonpolar facets, similar to the growth of secondary NWs in the ZNBs, will transform most the exposed nonpolar facet into polar facet (Stage B of scheme 2). After that, the SO_4^{2-} ions substitute for hydroxyl anions again and hinder the attachment of growth units of $[\text{Zn}(\text{OH})_4]^{2-}$ onto these (0001) polar facets of the secondary grown nanostructures directing the growth sideways. It is basically growing secondary ultra-thin sheets from the nonpolar side facets of the initial ZNWs (Stage C of scheme 2). The secondary ultra-thin sheets keep on growing until the final structure takes a leaf shape (Stage D of scheme 2).



Scheme 2. A scheme showing the formation of a ZnO nanoleaf from initial ZNW.

The optical properties of the as-grown ZnO structures with different morphologies were investigated by analyzing their room-temperature PL spectra shown in Figure 4. From the curves, we can see two bands for each nanostructure. The first is a luminescence band centered at 386 nm and the second is a broadband in the region of 450-850 nm. The six investigated nanostructures evidently show the following intensity order for the broad luminescence band: ZNFs > ZNLs > HZNDs > ZNBs > ZNDs > ZNWs. For the peak centered at 386 nm, ZNWs have the relatively highest intensity. In general, these PL spectra are similar to the ZnO PL spectra reported in literature.^{19,20} The peak centered at 386 nm (3.22 eV) is generally attributed to the near band-edge emission of ZnO (3.37 eV) and the recombination of free excitons. On the other hand, it was reported that the broad band in the visible light region is a result of the oxygen vacancies at the surface of ZnO.^{19,20}

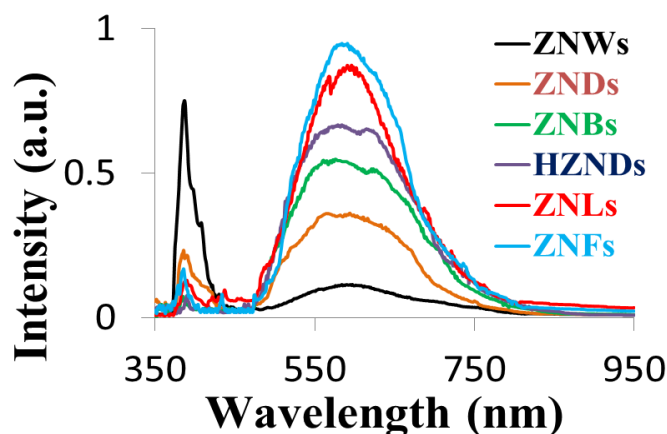


Figure 4. PL spectra of the different ZnO morphologies.

It was reported that the surface properties of metal oxides such as heterogeneous catalysis, corrosion inhibition and gas sensing are significantly affected by the defects at their surfaces.²¹⁻²² many studies can be found on the theoretical calculations and experimental data regarding the role that the intrinsic defects play in the chemistry of ZnO surface and the chemisorption effects.^{22,23} Moreover, the mechanism behind the oxygen vacancies induced enhancement in gas sensing capabilities of ZnO has been investigated.²⁴ The interaction between ZnO surfaces having high density of oxygen vacancies and gas molecules is improved by greatly due to the high surface adsorption of oxygen on these surfaces.

The visible region intensity attributed to the density of oxygen vacancies varies with different ZnO morphologies, ZNFs > ZNLs > HZNDs > ZNBs > ZNDs > ZNWs. The correlation between the green band emission and the morphology of ZnO structure was investigated in a study that concluded that the highest green band intensity corresponded to the morphology with the highest surface-to-volume ratio (the highest density of surface oxygen vacancies).²⁰ In this study, the BET analysis for the different nanostructures was performed and the surface area

measured for the ZNFs, ZNLs, HZNDs, ZNBs, ZNDs and ZNWs are 49.2, 44.8, 53.3, 41.6, 25, and 23.5 m²g⁻¹, respectively. Clearly, the ratio of the surface-to-volume of the grown hierarchical ZnO nanostructures is much higher than that of their initial mono-morphological ZNDs and ZNWs. These observations strongly suggest that there is a strong correlation between the density of oxygen vacancies and the surface-to-volume ratio of ZnO and agree with the conclusions of the previous study in the literature.²⁰

Nevertheless, the surface-to-volume ratios of the ZNFs and ZNLs are comparable and less than that of the HZNDs and still show larger oxygen vacancies. The morphological and structural analyses of the different grown structures performed and discussed earlier indicate that this is due to the increased population of exposed polar facets in the ZNFs and ZNLs.

Gas sensing properties

Hierarchically designed ZnO nanostructures with high surface-to-volume ratios hold many promises as high performance gas sensors. Furthermore, the creation of junctions between the initial ZnO nanostructure and secondary nanostructure is known to enhance the density of active sites and improve the gas sensing properties in general.¹⁴ The increase in the polar exposed facets after growing secondary nanostructures on the initial ZNW with totally nonpolar exposed facets is another reason to improve the gas sensing properties as discussed earlier.¹⁸ For the above mentioned aspects, the produced hierarchically designed nanostructures are likely to perform highly as gas sensors in comparison with the mono-morphological nanostructures.

Six different types of gas sensors have been fabricated based on ZNWs, ZNDs, ZNBs, HZNDs, ZNLs and ZNFs. All the fabricated devices are based on single nanostructure. The operating temperature is known to have a great impact on the sensitivity of ZnO gas sensors, therefore all sensors have been tested at a range of temperatures to figure out the optimum one for acetone detection. Figure 5 shows the responses of the three different sensors to 200 ppm acetone as a function of the operating temperature. It is noted that the tested sensors become more sensitive as the operating temperature increases up to a certain temperature value and then become less sensitive to acetone with a further increase in temperature. ZNW, ZND, ZNB, HZND, ZNL and ZNF sensors showed their highest sensitivity at 325, 375, 400, 425, 400, and 425 °C respectively. This observation can be explained as follow. This type of metal oxide sensors require enough thermal energy to activate. At low operating temperature, the chemical activation is not enough causing the sensitivity to be low as well. On the other hand, at relatively very high operating temperatures, the activation is improved significantly and acetone molecules that are adsorbed on the nanostructure surface are forced to leave the surface before exchanging charges. Consequently, sensors are less sensitive at relatively high operating temperatures.

The difference in optimum operating temperature of the tested sensors may originate from their different oxygen absorption

capabilities. From room temperature, the conductivity of the nanostructure increases as the operating temperature starts to increase due to the enhanced density of thermally excited electrons. After sometime and around 175 °C, the conductivity of the nanostructure shows signs of decrease due to chemisorption of oxygen on its surface which lowers the density of electrons in the conduction band of ZnO. The two opposite processes which are thermal excitation and oxygen chemisorption processes keep on going with two opposite effects until chemisorbed oxygen species cover the entire surface of ZnO nanostructure causing the optimum sensor response. After this level of operating temperature, the process of electrons thermal excitation prevails and no more oxygen can be adsorbed leading to lower sensor response. Figure 5 shows that the order of the optimum operating temperature of the six sensors $(ZNF)_{Temp} > (HZND)_{Temp} > (BNW)_{Temp} > (ZNL)_{Temp} > (ZND)_{Temp} > (ZNW)_{Temp}$, which the same order of their ability to absorb oxygen species as confirmed by the PL analysis except for ZNL sensor. Hence, we suggest that the optimum operating temperature of gas sensors depends greatly on nanostructure capability to absorb oxygen. The ZNL exception could be due to the extra self-heating caused by the current passing through the relatively ultrathin sheets of ZNL.²⁵

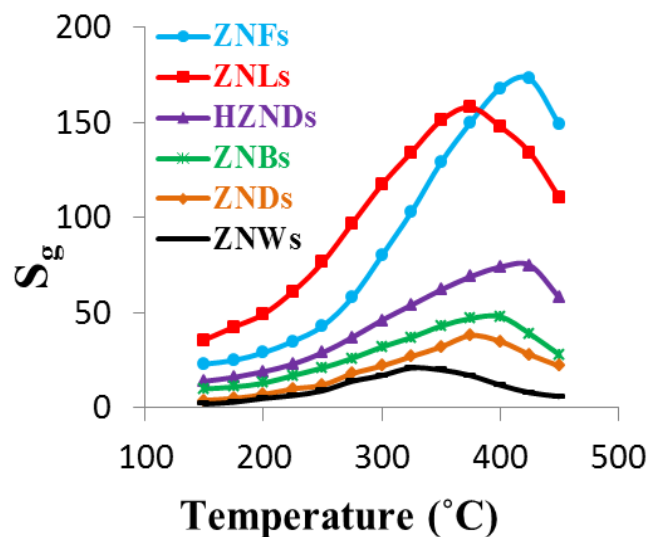


Figure 5. Sensor response versus operating temperature curves of the six sensors at 200 ppm of acetone.

The sensitivity of the six gas sensors as functions of acetone concentration as represented by the curves is shown in figure 6. All sensors were tested at their optimum operating temperature. At all acetone concentration levels, the order of sensors responses is as follow: ZNFs > ZNLs > HZNDs > ZNBs > ZNDs > ZNWs. The ZNF sensor showed the highest sensitivity, while the lowest sensitivity was shown by the ZNW sensor. It is obvious that sensors fabricated based on hierarchical nanostructures are more sensitive than those of the initial mono-morphological nanostructures over the entire range

of acetone concentrations. Furthermore, hierarchical nanostructures assembled from 2D nanostructure building blocks with more exposed polar facets are more sensitive than hierarchical nanostructures assembled from 1D nanostructure building blocks with more exposed nonpolar facets.

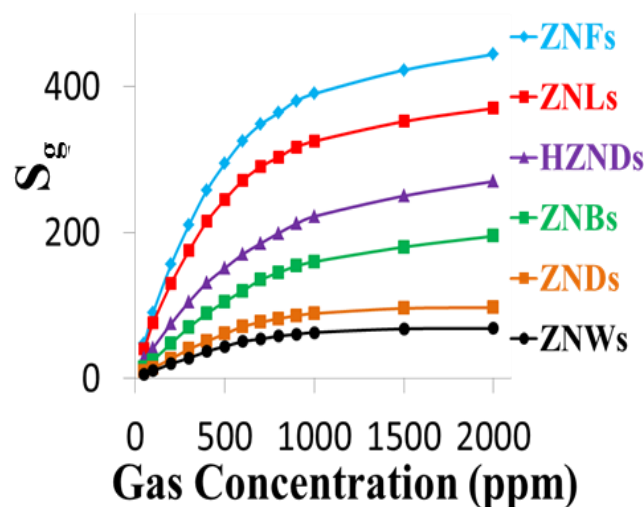


Figure 6. Sensor response as function of acetone concentration of the six sensors.

Beyond concentration values of 1000 ppm, sensors that are fabricated based on mono-morphological nanostructures started to saturate. On the other hand hierarchically designed sensors did not saturate until concentration value of 2000 ppm. This observed phenomenon originates from the following concept. When the number of gas molecules is small in comparison with adsorbing sites on the surface of the nanostructure, the reaction between them is the rate-determining step. The relationship between the sensitivity and gas concentration is linear. Consequently, nanostructures with higher density of adsorption sites on their surfaces like hierarchical nanostructures in this case saturate at higher levels of gas concentration.

The response characteristics of the six fabricated ZnO sensors to 100 ppm acetone are shown in figure 7. The response times of ZNW, ZND, ZNB, HZND, ZNL, and ZNF sensors are 10, 9, 3, 2, 5 and 2 s, respectively, while the recovery times are 15, 14, 6, 4, 9 and 4 s, respectively. Evidently, sensors fabricated based on hierarchical nanostructures are faster than those based on mono-morphological nanostructures. Also, ZNF and HZND sensors showed the fastest responses among all sensors which could be a result of their higher operating temperature. Comparing the obtained response time values with those reported previously in the literature ranging from 30 to 500 s, one can see the significant improvement in using hierarchical nanostructures in gas sensing.^{26,27}

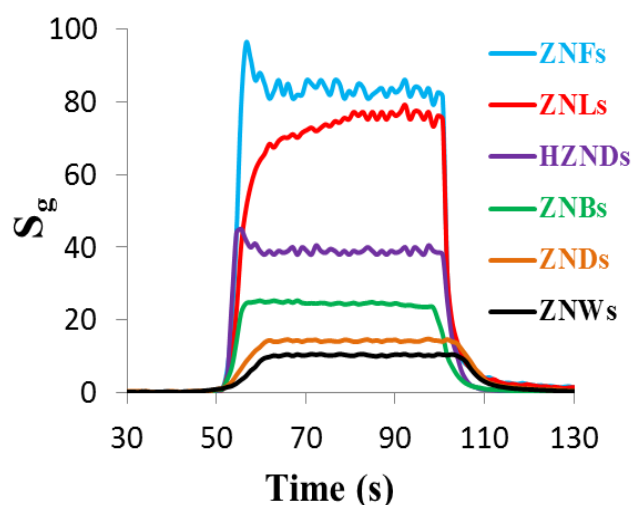


Figure 7. Sensor response characteristics of the six sensors to 100 ppm of acetone.

The detection limit of all fabricated sensors was investigated by recording their responses to acetone concentration levels ranging from 50 ppb to 1 ppm. The response of the sensor fabricated based on a single ZNL tested at 375 °C is shown in figure 8. Only the ZNL sensor was able to sense at this range of concentration levels. In fact, it showed a reliable and impressive performance in comparison not only to the other tested sensors in this study but also to those reported previously in the literature.^{26,27} The response time and recovery time of the ZNL sensor to 1 ppm acetone are about 12 and 16 s, respectively.

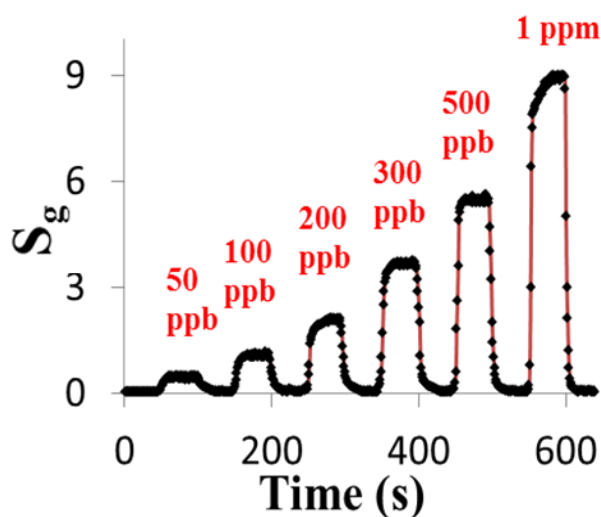


Figure 8. Sensor response versus time curve of the ZNL sensor in the range of (0.05–1 ppm).

The sensing mechanism of the fabricated ZnO gas sensors mainly depends on the impact of adsorption and desorption

processes of gas molecules on the surface of exposed sensing material. Using the depletion region modulation model, the mechanism can be described as follow.²⁸ At ambient conditions, oxygen species are adsorbed on the surface of ZnO nanostructures and interact with free electrons from the conduction band. As a result of this interaction, chemisorbed oxygen species including O_2^- , O^- , and O^{2-} are formed. Once acetone gas is presented, its molecules undergo oxidation process with the adsorbed oxygen on the surface of ZnO. As a result of the oxidation process, previously captured electrons will be liberated and sent back to the conduction band of ZnO nanostructure as represented in Eq. (1).²⁹



The enhanced performance of ZnO gas sensors can be explained by considering surface defects. The PL analysis showed that there is a higher surface defects density in the hierarchical nanostructures in comparison with their monomorphological counterparts for several reasons including the higher surface-to-volume ratio and the creation of many junctions between the secondary and initial nanostructures, which are thought of as the active sites that can improve the sensitivity.³⁰ Moreover, the PL analysis proved that nanostructures with more exposed polar facets possess higher density of surface defects. So, hierarchical nanostructures with more exposed polar facets such as ZNFs and ZNLs have a higher concentration of electron donor induced oxygen vacancy defects, resulting in the formation of more surface oxygen species. In other words, in ZNFs and ZNLs a higher density of electrons will be captured from the conduction band creating a larger depletion region.

The superior gas sensing properties of ZNFs and ZNLs over the HZNDs and ZNBs can be attributed the polarity of their exposed facets since they have comparable or even less surface-to-volume ratios. It was reported that absorption of oxygen species and gas molecules depend significantly on the surface atomic structures.¹⁴ The positive termination of (0001) facet improves the capability of absorbing O_2 physically or chemically because of the unsaturated oxygen coordination. Therefore, the (0001) facet possesses the highest chemisorption capability.

ZNFs and ZNLs are assembled from 2D ZnO nanostructure building blocks and the dominating exposed facets are the (0001) ones, which enhance their gas sensing properties greatly. On the other hand, HZNDs and ZNBs are assembled from 1D ZnO nanostructure building blocks and the dominating exposed facets are the nonpolar $\{10\bar{1}0\}$ planes, which does not allow their gas sensing properties to be as good as those of ZNFs and ZNLs.

Conclusions

In conclusion, novel hierarchical ZnO nanostructures with different fractions of exposed polar facets were rationally synthesized on a large scale through a simple and economical

hydrothermal route. Control experiments revealed that the formation of these hierarchical structures depends significantly on the type of the zinc counter-ions. Essentially, the grown hierarchically structured ZnO have displayed a strong structure induced enhancement of gas sensing performance toward acetone and fast response compared to that of their monomorphological counterparts. This is primarily attributed to their high surface-to-volume ratio, increased population of active (0001) exposed facets as well as the creation of junctions between the secondary and initial nanostructures. The presented technique to produce hierarchical ZnO nanostructures with rational control over their morphology and size is also expected to be useful for other applications such as dye-sensitized solar cells and photocatalysis.

Acknowledgements

M. R. Alenezi thanks the Public Authority of Applied Education and Training (PAAET) and the Government of the State of Kuwait for their financial support.

Notes and references

^aCollege of Technological Studies, Public Authority for Applied Education and Training, P.O. Box 42325 Shuwaikh, Kuwait

Email: mr.alenezi@paaet.edu.kw

^bDepartment of Physics, College of Science, University of Hail, P.O. Box 2440, Hail, KSA

^cNanoelectronics Center, Advanced Technology Institute, University of Surrey, Guildford, GU2 7XH, UK

- Z. Wang, J. Gong, Y. Su, Y. Jiang, S. Yang, *Crystal Growth & Design*, 2010, **10**, 2455–2459.
- K. D. G. I. Jayawardena, C. Opoku, J. Fryar, S. R. P. Silva, S. J. Henley, *Applied Surface Science*. 2010, **257**, 5274–5277.
- M. McCune, W. Zhang, Y. Deng, *Nano Lett.*, 2012, **12**, 3656–3662.
- M. R. Alenezi, *International Journal of Engineering Sciences & Research Technology*, 2014, **7**, 755–758.
- S. Chen, G. Sun, *ACS Appl. Mater. Interfaces*, 2013, **5**, 6473–6477.
- M. Zhang, C. Shao, Z. Guo, Z. Zhang, J. Mu, T. Cao, Y. Liu, *ACS Appl. Mater. Interfaces*, 2011, **3**, 369–377
- Y. Qin, X. D. Wang, Z. L. Wang, *Nature* **2008**, *451*, 809–813
- H. Yang, L. Hao, N. Zhao, C. Du, Y. Wang, *CrystEngComm*, 2013, **15**, 5760–5763.
- M. Righettoni, A. Tricoli, S. E. Pratsinis, *Anal. Chem.* 2010, **82**, 3581–3587.
- Yang, P. D.; Yan, H. Q.; Mao, S.; Russo, R.; Johnson, J.; Saykally, R.; Morris, N.; Pham, J.; He, R. R.; Choi, H. Controlled Growth of ZnO Nanowires and Their Optical Properties. *J. Adv. Funct. Mater.* 2002, **12**, 323–331.
- D. Moore, Y. Ding, Z. L. Wang, *Angew. Chem., Int. Ed.* 2006, **45**, 5150–5154.
- P. X. Gao, Z. L. Wang, *Appl. Phys. Lett.* 2004, **84**, 2883–2886.
- Z. R. R. Tian, J. A. Voigt, J. Liu, B. McKenzie, M. J. McDermott, M. A. Rodriguez, H. Konishi, H. F. Xu, *Nat. Mater.* 2003, **2**, 821–826.
- M. R. Alenezi, S. J. Henley, N. G. Emerson, S. R. P. Silva, *Nanoscale*, 2014, **6**, 235–247.
- M. R. Alenezi, A. S. Alshammari, P. D. Jarowski, Talal H. Alzanki, S. J. Henley, S. R. P. Silva, *Langmuir*, 2014, **30**, 3913–3921.
- M. R. Alenezi, T. H. Alzanki, A. M. Almeshal, *International Journal of Science and Research*. 2014, **3**, 588–591.
- X. Zhou, Z. X. Xie, Z. Y. Jiang, Q. Kuang, S. H. Zhang, T. Xu, R. B. Huang and L. S. Zheng, *Chem. Commun.*, 2005, 5572–5574.
- M. R. Alenezi, A. S. Alshammari, K. D. G. I. Jayawardena, M. J. Beliatas, S. J. Henley and S. R. P. Silva, *J. Phys. Chem. C*, 2013, **117**, 17850–17858.
- X. L. Wu, G. G. Siu, C. L. Fu and H. C. Ong, *Appl. Phys. Lett.*, 2001, **78**, 2285–2288.
- T. Andelman, Y. Y. Gong, M. Polking, M. Yin, I. Kuskovsky, G. Neumark, S. O'Brien, *J. Phys. Chem. B*, 2005, **109**, 14314–14318.
- G. A. Gutierrez-Sosa, A. Baraldi, R. Larciprete, S. Lizzit, *J. Am. Chem. Soc.* 2002, **124**, 7117–7122.
- R. Lindsay, E. Michelangeli, B. G. Daniels, T. V. Ashworth, A. J. Limb, H. Geistlinger, *J. Appl. Phys.* 1996, **80**, 1370–1381.
- S. Polarz, A. Roy, M. Lehmann, M. Driess, F. E. Kruijs, A. Hoffmann, P. Zimmer, *Adv. Funct. Mater.* 2007, **17**, 1385–1391.
- L. Liao, H. B. Lu, J. C. Li, H. He, D. F. Wang, D. J. Fu, C. Liu, W. F. Zhang, *J. Phys. Chem. C* 2007, **111**, 1900–1903.
- H. G. Moon, Y. Shim, D. H. Kim, H. Y. Jeong, M. Jeong, J. Y. Jung, S. M. Han, J. K. Kim, J. Kim, H. Park, J. Lee, H. L. Tuller, S. Yoon, H. W. Jang, *Scientific reports*, 2012, **2**:588.
- Y. K. Jun, H. S. Kim, J. H. Lee, S. H. Hong, *Sens. Actuator B*, 2006, **120**, 69–73.
- P. S. Cho, K. W. Kim, J. H. Lee, *J. Electroceram.*, 2006, **17**, 975–978.
- Z. H. Jing and J. H. Zhan, *Adv. Mater.*, 2008, **20**, 4547–4551.
- P. A. Murade, V. S. Sangawar, G. N. Chaudhari, V. D. Kapse and A. U. Bajpeyee, *Curr Appl. Phys.*, 2010, **11**, 451–456.
- D. H. Zhang, Z. Q. Liu, C. Li, T. Tang, X. L. Liu, S. Han, B. Lei and C. W. Zhou, *Nano Lett.*, 2004, **4**, 1919–1924.